Piezoelectric Transduction of a Wavelength-Scale Mechanical Waveguide

Yanni D. Dahmani, Christopher J. Sarabalis,* Wentao Jiang, Felix M. Mayor, and Amir H. Safavi-Naeini†

Department of Applied Physics and Ginzton Laboratory, Stanford University, 348 Via Pueblo Mall, Stanford, California 94305, USA

(Received 3 August 2019; revised manuscript received 22 November 2019; accepted 24 January 2020; published 25 February 2020)

We present a piezoelectric transducer in thin-film lithium niobate that converts a 1.7-GHz microwave signal to a mechanical wave in a single mode of a 1-μm-wide waveguide. We measure a -12-dB conversion efficiency that is limited by material loss. The design method we employ is widely applicable to transduction in wavelength-scale structures in emerging phononic circuits such as those needed for efficient piezo-optomechanical converters and spin-phonon transducers.

DOI: 10.1103/PhysRevApplied.13.024069

I. INTRODUCTION

Phonons interact strongly and coherently with many kinds of degrees of freedom and so can glue together hybrid classical and quantum systems. With efficient electromechanical transducers, we can leverage microwave electronics to read out and control quantum dots [1,2], color centers [3,4], magnons [5], and optical photons [6–16]. Furthermore, the phonons themselves are useful for manipulating classical and quantum information. Ultrahigh-Q nanomechanical resonators [17] have precipitated a number of new approaches to hardware-efficient quantum information processing [18,19]. Since mechanical waves are highly confined and slow compared with light, they are apt for low-loss compact microwave components for storing [20–22], routing [23], delaying [24–26], and filtering [27–29] classical and quantum information.

Many of these applications rely on or benefit from going to smaller mechanical waveguides and resonators. Per phonon, the strain and displacement in a cavity and in a waveguide scale as the reciprocal of the square root of the volume and of the area, respectively. As a result, size plays a central role in improving phonon coupling rates in optomechanics [30–34] and strain-coupled two-level systems [35]. Moreover, wavelength-scale structures have fewer modes, giving more control over loss and coupling. The smaller the waveguide or resonator the better, placing new demands on the design of efficient and mode-selective electromechanical transducers [36–38]. While piezoelectric driving of wavelength-scale structures—both nanobeam resonators [11,13–15,39] and waveguides [7,40]—has been demonstrated, many devices, such as nanophotonic acousto-optic modulators [7] and microwave-to-optical quantum converters [14,15], are still primarily limited by the efficiency of their transducer. An important challenge remains in systematically designing and characterizing wavelength-scale single-mode transducers as standalone phononic components that can be widely incorporated into phononic networks.

Here we present a piezoelectric transducer operating at 1.7 GHz that excites the fundamental horizontal shear (SH0) mode of a 1-μm-wide waveguide in thin-film lithium niobate (LN). We have recently used such transducers to drive the breathing mode of a nanobeam, increasing our previously demonstrated electromechanical efficiency by five orders of magnitude [41].

Our work focuses on a single transducer design for our platform, but many of the methods we employ are general. In Sec. II, we show how the area of a transducer can be estimated from the piezoelectric coupling coefficient k^2_{eff} and the target bandwidth. With a large k^2_{eff}, a small transducer can be matched to 50 Ω, making it easier to couple it to a wavelength-scale waveguide. In Sec. III, we show that, for shear waves, adiabatic elastic horns cannot be used to generate wide beams. This motivates our narrow designs. In Sec. IV, we formulate the design problem in terms of the electromechanical scattering matrix and show how the elements of the matrix (in particular, the transmission $t_{b\mu}$) can be computed by the finite-element method (FEM) with a normal mode decomposition. This S-matrix approach makes it possible to incorporate the transducer into a more general network of microwave electromagnetic and phononic components. In our analysis, we find that the best-matched transducer is not the most efficient; microwave reflections $|S_{11}|$ cannot be used as a proxy for $|t_{b\mu}|$. For this reason, our measurements presented in Sec. V focus on deembedding the transducer from a cascaded transducer-waveguide-transducer network, giving us a conversion efficiency $|t_{b\mu}|^2 = 7.0\%$.

*sicamor@stanford.edu
†safavi@stanford.edu

II. PIEZOELECTRIC-COUPLING CONSTRAINTS ON TRANSDUCER AREA

We begin by considering the area A on the surface of a chip needed to impedance match a transducer to a 50 Ω transmission line. The smaller we can make our transducer, the easier it will be to couple it to a wavelength-scale waveguide, but the area of the transducer is constrained by the impedance of the transmission line, the desired bandwidth, and the piezoelectric coupling coefficient k^2_{eff}. We show in Appendix A that for a few different models of piezoelectric transducers, these important parameters are related by the equation

$$A = \frac{\pi}{4}\frac{1}{\omega_s^2 c_s k^2_{\text{eff}}}\int d\omega\, G(\omega) \tag{1}$$

$$= \frac{\pi^2}{8}\frac{G_0}{\omega_s^2 c_s}\frac{\gamma}{k^2_{\text{eff}}} \quad \text{[for Lorentzian } G(\omega)\text{]}. \tag{2}$$

Here, G is the conductance (the real part of the admittance Y) of the interdigitated transducer (IDT); c_s is the capacitance per unit area; ω_s is the series resonance frequency; G_0 and γ are the maximum and full width half maximum, respectively, of $G(\omega)$; and the integral is evaluated over an interval around ω_0.

Equation (1) gives us a quick way to estimate device parameters. We see that matching to 50 Ω over a large bandwidth comes at the cost of area. Materials such as LN with a high $\varepsilon k^2_{\text{eff}}$, where ε is the dielectric permittivity, enable small transducers with a large bandwidth. If we only need a small bandwidth, we can make a small resonant transducer that is easier to couple to a wavelength-scale waveguide. In principle, there is no lower bound on the area of a 50-Ω-matched transducer; in practice, material and clamping losses set a minimum on γ.

Horizontal shear (SH) waves in a LN slab are strongly piezoelectric, enabling small transducers. SH waves traveling along the Y crystal axis in X-cut LN couple to an IDT's electrodes mainly via the $d_{YZY} = 68$ pC/N component of the piezoelectric tensor [42,43], leading to a large k^2_{eff} of up to 35%. The coupling coefficient can be computed for an arbitrary mode of a unit cell of an arbitrary IDT as shown in Appendix B; values for various modes of a LN slab without electrodes were reported by Kuznetsova *et al.* [44].

A 1.9-μm-pitch IDT with $c_s = 155$ μF/m^2 and $\omega_s = 2\pi \times 1.7$ GHz (computed by the FEM) requires an area of roughly 250 μm^2 to match it to 50 Ω over 10 MHz. This bandwidth is consistent with our previous measurements of loss, which place a lower bound on the bandwidth for the platform [45]. With this area constraint in hand and the intuition that comes with it, we turn our attention to the modes of LN waveguides and the physics of elastic horns.

III. MODES OF A LN WAVEGUIDE AND ELASTIC-HORN DESIGN

A piezoelectric waveguide with continuous translational symmetry, such as the rectangular waveguide shown in Fig. 1(d), supports a power-orthogonal basis of modes at each frequency ω. These modes solve an eigenvalue problem on a two-dimensional cross section of the waveguide in which the stress field σ and the velocity field $\mathbf{v}$ of the theory of elasticity and the electrostatic potential Φ

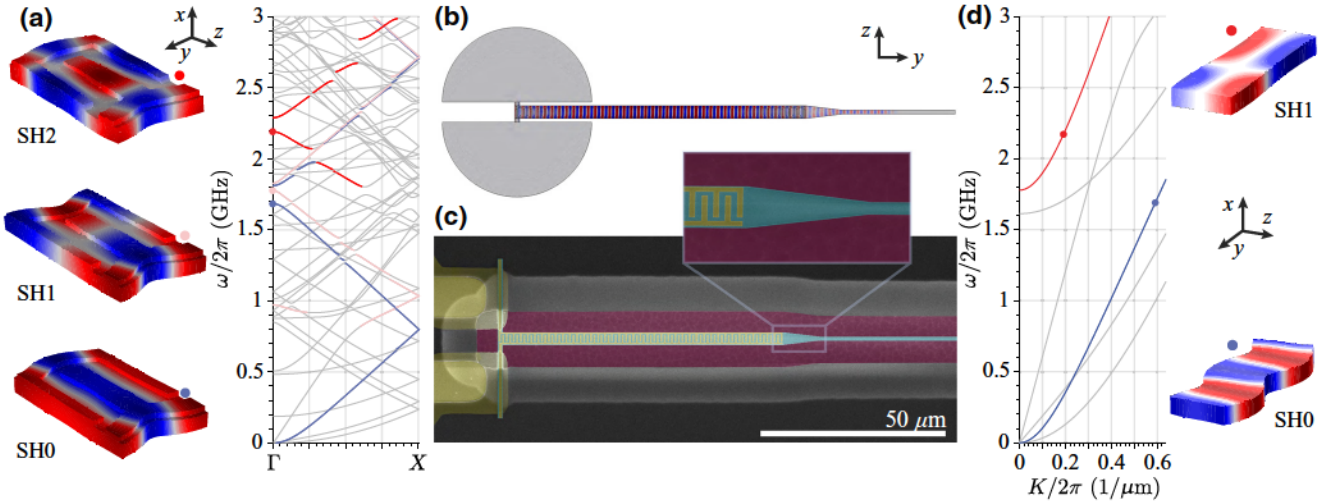

FIG. 1. Suspended transducers patterned in 300-nm-thick X-cut LN on silicon, designed to excite the SH0 mode of a 1-μm-wide waveguide at 1.7 GHz. They comprise an aluminum IDT 3.4 μm wide and 100 nm thick, and a 10-μm-long linear horn. In the false-color SEM image (c), LN is blue, aluminum is yellow, and the XeF_2 release etch front is burgundy. FEM analysis (b) shows that the horn scatters the SH0 mode of the IDT efficiently into the SH0 mode of the 1-μm-wide waveguide. The bands and Bloch functions of the IDT and waveguide which constitute the asymptotic state of the horn are plotted on the left (a) and right (d), respectively. Waves propagate along y, and the colors indicate the displacement along z.

of electrostatics are coupled by the piezoelectric tensor $\mathbf{d}$. The modes $|\psi_m\rangle \equiv (\boldsymbol{\sigma}_m, \mathbf{v}_m, \Phi_m)$, indexed by m, vary along the waveguide as $e^{iK_m y}$, with a complex eigenvalue K_m. If $K_i \neq K_j^*$, modes i and j are power-orthogonal and satisfy

$$\langle \psi_i | \, \psi_j \rangle \equiv \int d\mathbf{S} \cdot \left(-\boldsymbol{\sigma}_i^* \mathbf{v}_j - \boldsymbol{\sigma}_j \mathbf{v}_i^* + i\omega \mathbf{D}_i^* \Phi_j - i\omega \mathbf{D}_j \Phi_i^* \right) = 0, \tag{3}$$

forming an inner-product space in which band structures can be computed and scattering can be studied [46]. Here $\mathbf{D} = -\boldsymbol{\varepsilon} \nabla \Phi + \mathbf{d}\boldsymbol{\sigma}$ is the electric displacement field, and we normalize our basis such that $\langle \psi_i | \, \psi_j \rangle = \delta_{ij}$. For more detail on our choice of Fourier conventions and the relationship between the inner product and power, see Appendix C.

The wavelength-scale LN waveguide we are trying to excite is 1 μm wide and 300 nm thick. It supports four modes between 0 and 1.6 GHz: the Lamb mode (A0), the horizontal shear mode (SH0), the first excited Lamb mode (A1), and the longitudinal mode (S0) [47]. The band structure is plotted in Fig. 1(d).

From Sec. II, we know we need a 250-μm^2 IDT and a way to couple it efficiently to the waveguide. A wider IDT provides room for the wires and reduces the impact of material loss (see Sec. IV). A natural choice is then to expand the mode of the narrow waveguide using a horn structure to couple it to a wider IDT. In microwave and acoustic design, adiabatic horns are commonly used to expand a beam, but elastic media have an added phenomenon that spoils this approach: they support surface waves.

If we increase the width of the waveguide adiabatically, the SH0 mode splits and becomes localized at the edges. This is analogous to how Rayleigh waves are localized at a surface. In Fig. 2(a), we vary the width of the waveguide and compute the wave vectors of the SH modes. The SH0 and SH1 modes of the 1-μm-wide waveguide (left) continuously transition to degenerate antisymmetric and symmetric edge modes, respectively (right). For shear waves, adiabatic horns cannot produce wide uniform beams and therefore cannot efficiently convert these waves from waves in a wide IDT to waves in a narrow waveguide.

We choose 3.4 μm for the width of the IDT so that an adiabatically tapered horn can efficiently scatter the transduced mode into the 1 μm waveguide. The narrow IDT allows us to simplify the design, make full use of the width of the transducer, spectrally resolve the SH0 and SH1 modes, and keep spurious shear modes in cutoff.

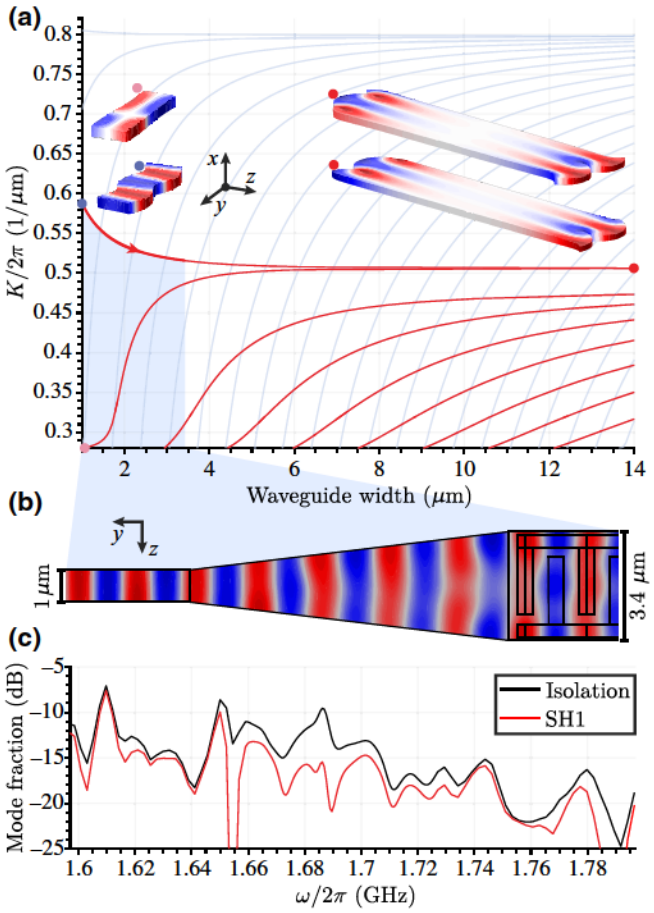

FIG. 2. (a) Adiabatic elastic horns do not generate wide mechanical beams. The SH0 and SH1 modes (u_z plotted at left) transition to degenerate antisymmetric and symmetric edge supermodes, respectively (right). Below 5 μm, the SH waves (red) are well resolved. The Lamb waves are plotted in light blue. (b) A linear horn scatters the SH0 mode of the 3.4-μm-wide IDT efficiently into SH0 of the 1-μm-wide output waveguide. (c) By decomposing the power in the waveguide, we find that transduction of spurious modes, i.e., the isolation, is better than -10 dB away from the nodes in the conductance over a 200-MHz bandwidth. The largest spurious component is the SH1 mode, plotted in red.

IV. FEM MODELS OF THE TRANSDUCER: LOSS LIMITS THE TRANSMISSION $t_{b\mu}$

A transducer is often sufficiently characterized by its admittance $Y(\omega)$, and the design objective may be to minimize microwave reflections, i.e., to match it to a transmission line. This is true, for example, when loss channels such as scattering into the bulk can be ignored and the mode structure of the radiation is well understood. But the admittance does not fully characterize the linear response; minimizing microwave reflections does not necessarily maximize the electromechanical transmission. Our numerical analysis presented in this section and the measurements presented in Sec. V are tailored to maximize and characterize the transmission into the SH0 mode, $t_{b\mu}$.

A three-dimensional FEM analysis of the transducer, as shown in Fig. 1(b), is used to solve the inhomogeneous piezoelectric equations at each frequency. The domain is

bordered by a perfectly matched layer. As discussed in Sec. III, the modes of the output waveguide form an inner-product space (see Appendix D) in which we decompose the power radiated by the IDT and check that the transducer excites a single mode. Given a solution $|\psi\rangle$, the coefficients a_m are computed using Eq. (3):

$$a_m = \langle \psi_m | \, \psi \rangle \,, \tag{4}$$

such that

$$|\psi\rangle = \sum_m a_m \, |\psi_m\rangle \,, \tag{5}$$

where $|a_m|^2$ is the power in mode m. For each mode m, there is an associated backwards-propagating mode $-m$, and this pair forms a piezoelectric port. In order to compute $t_{b\mu}$, we set the voltage across the IDT at each frequency ω, compute $Y(\omega)$ and a_m, and relate them to a column of the S-matrix, one component of which is $t_{b\mu}$. Details of piezoelectric ports and expressions for the S-matrix can be found in Appendix E.

Our transducer is a 1.92-μm-pitch 100-nm-thick aluminum IDT with a duty cycle of 50%. The IDT's fingers end 300 nm away from the 400-nm-wide bus wires that run along the edges of the waveguide. Based on previous measurements on our platform [45], we incorporate a uniform material loss tangent corresponding to $Q_i = 300$ and scale the piezoelectric tensor from its bulk values by 0.67. The SH0 and SH2 Γ-point modes of the IDT [Fig. 1(a)] are efficiently transduced and scattered into the SH0 and SH1 modes of the waveguide [Fig. 1(d)]. In what follows, we focus on the SH0 mode of the IDT but have recently used the SH2 response to drive the breathing mode of a nanobeam [41].

Our analysis in Sec. III suggests that the 10-μm-long linear horn shown in Fig. 2(b) will function approximately adiabatically. Over a large bandwidth, over 90% of the power transmitted into the waveguide is transmitted into the SH0 mode. Less than -10 dB goes into spurious modes [labeled "Isolation" in Fig. 2(c)]. Excluding the nodes in the conductance, the power in the largest spurious mode (SH1) remains below -15 dB over 200 MHz.

In Fig. 3, we analyze how impedance matching and damping contribute to $t_{b\mu}$ for transducers of different lengths. At first, as N increases, the microwave reflections drop and the transmission improves as expected. But improvements in matching to the transmission line compete with damping in the IDT. This is seen in the fraction of the dissipated energy which is lost due to intrinsic damping [Fig. 3(b)]. Above an optimal N, the transmission $t_{b\mu}$ decreases even as microwave reflections continue to drop. These competing effects lead to a maximum in $|t_{b\mu}|^2$ for an optimal N [Fig. 3(c)]: 12% for 29 finger pairs with

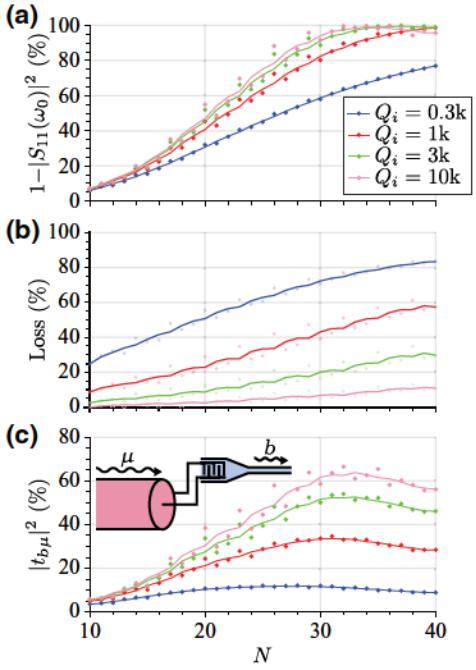

FIG. 3. By computing the linear response $Y(\omega)$ and decomposition $\{a_m\}$, we study the N-dependence of the transmission $t_{b\mu}$ from a 50 Ω transmission line to the SH0 mode. (a) Microwave reflections S_{11} decrease with N. Lower-loss devices are matched with smaller N. (b) As the reflections drop, the fraction of the total power lost increases, diminishing transmission into the SH0 mode. (c) These competing effects lead to an optimal N for maximizing $|t_{b\mu}|^2$, which increases with Q_i. Numerical results (points) are smoothed with a moving-window average (curve) for clarity.

$Q_i = 300$. In short, minimizing S_{11} does not always maximize $t_{b\mu}$. Also, $t_{b\mu}$ is larger in transducers with lower dissipation (larger Q_i).

For $Q_i = 300$, intrinsic damping in the transducer is the dominant loss channel, with only a small fraction of the energy lost to the tethers. Of the total power $2G(\omega)\,|V(\omega)|^2$ dissipated by an $N = 40$ transducer such as those measured in Sec. V, 11% is emitted into the waveguide, 96% of which is in the SH0 mode. Only 5% is lost to clamping by the tethers along the back edge, while the other 84% is lost to intrinsic damping.

There are a few approaches that can be used to improve $|t_{b\mu}|^2$ beyond 12%. The most obvious is to improve the material parameters k^2_{eff} and Q_i [Fig. 3(c)]. For applications in quantum science, operating at cryogenic temperatures will likely increase Q_i by suppressing thermally induced mechanical loss and ohmic dissipation in the electrodes. Another strategy is to reduce the reflection coefficient at the IDT-waveguide interface, reducing the influence of resonance and allowing us to make longer transducers before reaching loss limits. Lastly, we could diverge from the low-width low-density-of-states design and employ

wider waveguides, embracing the challenges of multimode design [39,40].

V. MEASUREMENTS

Starting with a 500-nm-thick film of LN on a 500-μm-thick silicon substrate, the film is thinned to 300 nm by argon milling before patterning an hydrogen silsesquioxane mask with e-beam lithography to define the waveguides. The mask is transferred to the LN by angled argon milling [15]. We then perform an acid clean to remove resputtered amorphous LN. We pattern the 100-nm-thick electrodes and 200-nm-thick contact pads by e-beam lithography and photolithography, respectively, followed by Al evaporation and liftoff. Finally, we release the structures with a masked XeF_2 dry etch.

The S-parameters of the transducers are measured with a vector network analyzer (Rhode & Schwarz ZNB20) on a probe station calibrated to move the reference plane to the tips of the probes (GGB nickel 40A). Several modes below 10 GHz are strongly transduced, as seen in S_{11} plotted in Fig. 4. The conductance $G \equiv \mathrm{Re}\, Y$ and susceptance $\chi \equiv -\mathrm{Im}\, Y$ for the SH0 mode plotted in Fig. 4(c) match well with the overlaid simulated curve and Γ-point frequency of the IDT unit-cell bands shown in Fig. 1(a). The peak conductance and full width half maximum for the SH0 mode, 6.5 mS and 9.7 MHz, respectively, inferred from a Lorentzian fit, agree with the results from our models, 6.9 mS and 7.3 MHz. We infer a static capacitance of 31 fF from a fit to the dc response of χ, and use it along with the conductance fitted and Eq. (2) to calculate a k^2_{eff} of 15%. (A value of 17% is computed in Appendix B). From the exact expression in Appendix A, we find $k^2_{\mathrm{eff}} = 12\%$ (14.6% simulated). This is decreased by the feedthrough capacitance of the contact pads.

In order to characterize the transducer, we need to extract $t_{b\mu}$ from measurements of S_{21}. To this end, we deembed the transducer from the transducer-waveguide-transducer two-port network by analyzing its response in the time domain. Consider a device with an $L = 200$ μm-long waveguide. If we were to infer $t_{b\mu}$ directly from the $|S_{21}|$ shown in Fig. 4(d) by halving the -15.7-dB peak, we would come to the unlikely conclusion that our transducer in practice is more efficient than in the simulation. This is because at 1.7 GHz, reflections at the IDT-waveguide interface resonantly enhance transmission through the waveguide. The transmission coefficient $t_{b\mu}$ cannot be deduced directly from the $|S_{21}|$ of a short device with large reflections at the IDT interface.

Instead, we isolate the propagation loss α and $t_{b\mu}$ by analyzing the time-domain impulse response $h(t)$, which is the inverse Fourier transform of $S_{21}(\omega)$, plotted for a device with $L = 800$ μm in Fig. 4(e). The first pulse takes the shortest path through the device and is attenuated by $|t_{b\mu}|^2 e^{-\alpha L/2}$. Each subsequent echo takes an additional

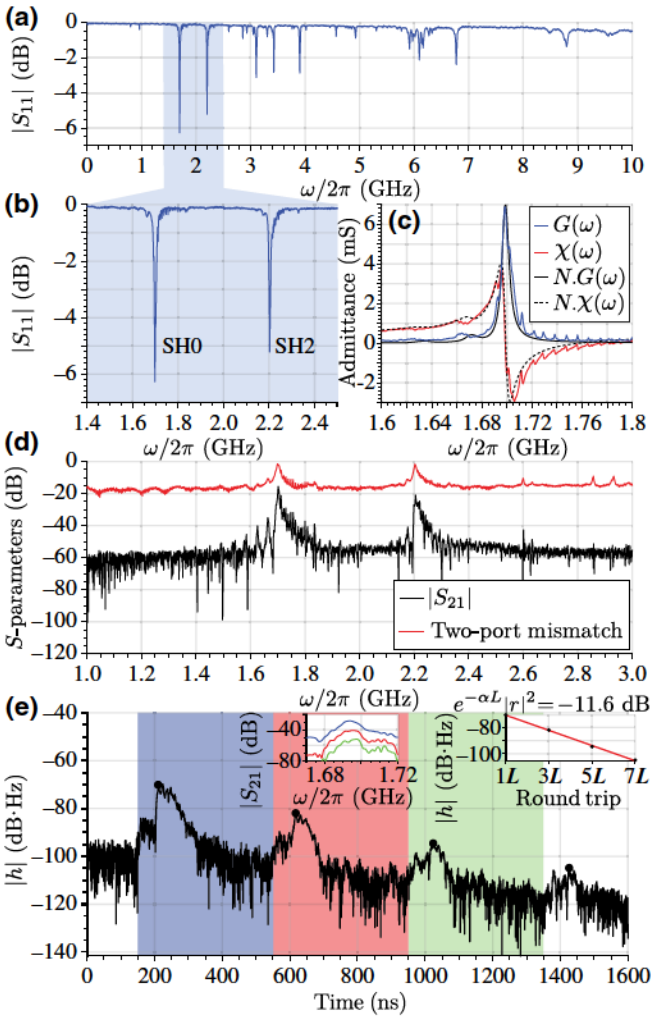

FIG. 4. (a) $|S_{11}|$ of an $N = 40$ transducer; (b) $|S_{11}|$ restricted to the SH0 and SH2 responses. (c) Conductance G and susceptance χ of the SH0 mode, overlaid on FEM results [labeled N.$G(\omega)$ and N.$\chi(\omega)$]. (d) $|S_{21}|$: for an ideal delay line with no insertion loss, this would equal the two-port mismatch $1 - |S_{11}|^2/2 - |S_{22}|^2/2$, shown in red (see Appendix G). (e) For $L = 800$ μm, the heights of the echoes in the impulse response are fitted (inset) to extract the round-trip loss. We filter the echoes (intervals shaded blue, red, and green) to compute the single-, triple-, and quintuple-transit S_{21}, plotted in corresponding colors (inset), used to extract $|t_{b\mu}|$ as described in Sec. V.

round trip, is attenuated by $|r|^2 e^{-\alpha L}$, and is delayed by $2L/v_g = 4.0 \times 10^2$ ns. We fit $|r|^2 e^{-\alpha L} = -11.6$ dB from the peaks in Fig. 4(e) and transform the first pulse (blue) back to the frequency domain (inset) to find $|t_{b\mu}|^2 e^{-\alpha L/2} = -28.6$ dB. More detail is provided in Appendix F.

The single-transit and round-trip loss are two constraints on three unknown quantities: $|t_{b\mu}|^2$, $|r|^2$, and α. By sweeping the length of the device, all three parameters can be determined independently. In lieu of a length sweep, we ignore scattering into other modes and assume $|t_{b\mu}|^2 + |r|^2 = 1$ at the IDT-waveguide interface to find a $|t_{b\mu}|^2$

of 7.0% (comparable to the simulated value of 8.9% for $N = 40$), an $|r|^2$ of 93%, and an α of 6.8 dB/mm.

Given the measured group velocity of $v_g = 4.0 \times 10^3$ m/s, this α corresponds to a quality factor $Q = \omega_0/\alpha v_g$ of 1700 in the waveguide and an f_0Q of 2.9×10^{12}, which is comparable to the results of our previous work on multimode high-frequency delay lines, with an f_0Q of 4.6×10^{12} [45]. We see an order-of-magnitude improvement over delay lines in suspended LN employing the S0 mode at 350 MHz, where $f_0Q = 0.45 \times 10^{12}$ [48]. Resonators using antisymmetric thickness modes exhibit f_0Q products over twice as large (9.15×10^{12}) [49].

VI. CONCLUSIONS

In suspended LN films, large reflections at the IDT-waveguide interface lead to resonance. These reflections distort signals in a filter or delay line and reduce bandwidth; here, resonance allows us to make small transducers and use simple horns to couple them to a waveguide. This reduced bandwidth can be tolerated in microwave-to-optical conversion and two-level system control and readout if it facilitates high conversion efficiency. At cryogenic temperatures, the intrinsic loss will likely drop, increasing the conversion efficiency of our design and enabling smaller bandwidths and therefore smaller transducers. At room temperature, the route to more efficient designs calls for wider transducers and efficient horns.

The design of a horn depends on the details of the given platform. For example, coupling surface acoustic waves to suspended waveguides and beams [39] introduces new features into the design such as mitigating reflections at the slab interface. The S-matrix formulation described here can be applied generally to design and characterize phononic components, such as horns, on a variety of platforms.

Our hope is that insights from our design of a phononic waveguide transducer in suspended LN can be generally applied to selectively exciting modes of wavelength-scale mechanical devices and that the methods we employ can inform approaches to the design and characterization of phononic components and systems.

ACKNOWLEDGMENTS

The authors would like to thank Rishi N. Patel, Patricio Arrangoiz-Arriola, and Timothy P. McKenna for useful discussions. This work is supported by a MURI grant from the U.S. Air Force Office of Scientific Research (Grant No. FA9550-17-1-0002), by a fellowship from the David and Lucille Packard foundation, and by the National Science Foundation through Grants No. ECCS-1808100 and No. PHY-1820938. Part of this work is performed at the Stanford Nano Shared Facilities (SNSF), supported by the National Science Foundation under Grant No. ECCS-1542152, and the Stanford Nanofabrication Facility (SNF).

Yanni D. Dahmani and Christopher J. Sarabalis contributed equally to this work.

APPENDIX A: RELATING THE PIEZOELECTRIC COUPLING COEFFICIENT TO THE NET CONDUCTANCE

In Sec. II, we relate the area of a transducer to the piezoelectric coupling coefficient k^2_{eff}, the static capacitance per unit area c_s, and the net conductance

$$A = \frac{\pi}{4}\frac{1}{\omega_0^2 c_s k^2_{\text{eff}}}\int d\omega\, G(\omega)\,, \tag{A1}$$

where the conductance is $G \equiv \text{Re}\, Y(\omega)$. In this appendix, we show how this expression holds for two very different models of piezoelectric transducers: the Butterworth–Van Dyke circuit model and the impulse response model of a surface-acoustic-wave (SAW) transducer [50]. We consequently take this expression as our device-independent and easily computable *definition* of k^2_{eff}.

1. Review of the Butterworth–Van Dyke model

The Butterworth–Van Dyke (BVD) circuit model is a simple and widely used model of a piezoelectric resonator. The circuit comprises a static capacitance C_0 in parallel with a motional series LC circuit, with motional inductance L_m and capacitance C_m. It is equivalent to the circuit in Fig. 5 with $R_m = 0$.

The BVD circuit, with admittance [51]

$$Y(\omega) = -i\omega C_0 - i\omega C_m \frac{1}{1-\omega^2/\omega_s^2}, \tag{A2}$$

exhibits a pole at the series resonance frequency $\omega_s \equiv 1/\sqrt{L_m C_m}$. Similarly, the impedance diverges at the parallel resonance frequency ω_p, where $Y(\omega_p) = 0$. Setting Eq. (A2) to zero and solving for ω_p, we find

$$\omega_p = \omega_s\sqrt{1 + \frac{C_m}{C_0}}. \tag{A3}$$

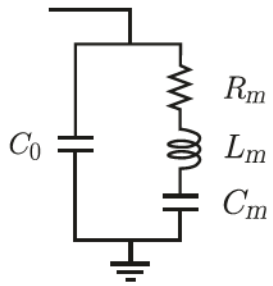

FIG. 5. Butterworth–Van Dyke circuit modified to include mechanical loss.

The splitting between the series and parallel resonance frequencies increases with the ratio of motional and static capacitance.

For a resonator, the effective piezoelectric coupling coefficient is defined in terms of the ratio of ω_s and ω_p [52,53]:

$$k_{\text{eff}}^2 = \frac{\pi}{2}\frac{\omega_s}{\omega_p}\left[\tan\left(\frac{\pi}{2}\frac{\omega_s}{\omega_p}\right)\right]^{-1}. \tag{A4}$$

To second order in $\left(\omega_p - \omega_s\right)/\omega_p$, the coupling coefficient is

$$k_{\text{eff}}^2 = \frac{\pi^2}{4}\frac{\omega_s}{\omega_p}\left(1 - \frac{\omega_s}{\omega_p}\right), \tag{A5}$$

as in Ref. [54], and to first order it is

$$k_{\text{eff}}^2 = \frac{\pi^2}{4}\left(1 - \frac{\omega_s}{\omega_p}\right). \tag{A6}$$

In the next section, we show that the motional capacitance C_m is proportional to the net conductance. Ultimately, we want to relate the net conductance, which is a convenient form for expressing design specifications, to the area of the transducer using intensive quantities such as ω_s, ω_p, and k_{eff}^2. To do this, it is helpful to note that the capacitance ratio in Eq. (A3),

$$\frac{C_m}{C_0} = \frac{\omega_p^2}{\omega_s^2} - 1, \tag{A7}$$

can be reexpressed to first order in $\left(\omega_p - \omega_s\right)/\omega_p$ as

$$\begin{aligned} k_{\text{eff}}^2 &= \frac{\pi^2}{8}\left(\frac{\omega_p^2}{\omega_s^2} - 1\right) \\ &= \frac{\pi^2}{8}\frac{C_m}{C_0}, \end{aligned} \tag{A8}$$

as in Ref. [55].

2. The modified Butterworth–Van Dyke circuit model

In order to relate the net conductance to C_m, we begin with the lossy resonator with motional resistance R_m shown diagrammatically in Fig. 5.

The admittance of this circuit,

$$\begin{aligned} Y(\omega) &= -i\omega C_0 + \frac{1}{1/ - i\omega C_m - i\omega L_m + R_m} \\ &= -i\omega C_0 + i\omega_s^2 C_m \frac{\omega}{\omega^2 + i\omega_s\omega/Q - \omega_s^2}, \end{aligned} \tag{A9}$$

is conveniently expressed in terms of the series resonance frequency $\omega_s \equiv 1/\sqrt{L_m C_m}$ and the quality factor $Q^{-1} \equiv \omega_s R_m C_m$. From Eq. (A9), we directly compute $G(\omega)$ and the net conductance relating it to k_{eff}^2 to derive Eq. (A1).

We can simplify the calculation by expanding the motional term as a sum of first-order poles

$$Y(\omega) = -i\omega C_0 + Y_+(\omega) + Y_-(\omega). \tag{A10}$$

The admittance of the pole at the frequency

$$\omega_\pm \equiv \pm\omega_s\sqrt{1 - 1/4Q^2} - i\omega_s/2Q \tag{A11}$$

is

$$Y_\pm(\omega) = \pm\frac{i\omega_s^2 C_m}{2\omega_0}\frac{\omega}{\omega \mp \omega_0 + i\omega_s/2Q}. \tag{A12}$$

For compactness, we introduce a modified series resonance frequency $\omega_0 \equiv \omega_s\sqrt{1 - 1/4Q^2}$.

Taking the real part of Y, we find the conductance

$$G(\omega) = G_+(\omega) + G_-(\omega), \tag{A13}$$

where

$$G_\pm(\omega) = \pm\frac{\omega_s^3 C_m}{4Q\omega_0}\frac{\omega}{(\omega \mp \omega_0)^2 + \omega_s^2/4Q^2}. \tag{A14}$$

The conductance is positive and even, i.e., $G(-\omega) = G(\omega)$.

Focusing on the positive pole, we recognize the net conductance as the mean of a Lorentzian by changing variables according to $\omega = \omega_s x/2Q$:

$$\begin{aligned} \int_{-\infty}^{\infty} d\omega\, G_+(\omega) &= \frac{\pi\omega_s^3 C_m}{4Q\omega_0} \\ &\quad\times\left[\frac{1}{\pi}\int_{-\infty}^{\infty} dx\, \frac{x}{(x - 2Q\omega_0/\omega_s)^2 + 1}\right] \\ &= \frac{\pi\omega_s^2 C_m}{2}. \end{aligned} \tag{A15}$$

Despite being an integral of the dissipation in the circuit, the net conductance is completely independent of R_m.

Each pole contributes $\pi\omega_s^2 C_m/2$ to the net conductance. Since the conductance is even,

$$\int_{-\infty}^{0} d\omega\, G(\omega) = \int_{0}^{\infty} d\omega\, G(\omega) \tag{A16}$$

$$= \frac{\pi\omega_s^2 C_m}{2}. \tag{A17}$$

By Eq. (A8), the coupling coefficient is

$$k_{\text{eff}}^2 = \frac{\pi}{4}\frac{1}{\omega_s^2 C_0}\int_0^\infty d\omega\, G(\omega) \tag{A18}$$

to first order in $(\omega_p - \omega_s)/\omega_p$. Devices are usually multimode. To exclude contributions to k^2_{eff} from other modes, we integrate $G(\omega)$ over a narrow band around ω_0.

In Eq. (A18), C_0 is the product of the static capacitance per unit area c_s defined in the text and the area of the transducer A. A simple rearrangement gives Eq. (1):

$$A = \frac{\pi}{4}\frac{1}{\omega_s^2 c_s k^2_{\text{eff}}}\int d\omega\, G(\omega)\,, \tag{A19}$$

where the integral is evaluated over an interval around ω_s.

Equations (A18) and (A19) use an approximate form for k^2_{eff}. We can write these expressions exactly using Eq. (A7):

$$\int d\omega\, G(\omega) = \frac{\pi}{2}\left(\omega_p^2 - \omega_s^2\right) C_0 \tag{A20}$$

and

$$A = \frac{2}{\pi}\frac{1}{\left(\omega_p^2 - \omega_s^2\right) c_s}\int d\omega\, G(\omega)\,. \tag{A21}$$

Without making any approximations, Eq. (A21) gives the area in terms of the net conductance and intensive quantities that can be easily calculated for a unit cell of a transducer (Appendix B).

Before moving on to the impulse response model, we consider the traditional BVD circuit discussed in Sec. A 1, which we encounter in Appendix B. In Eq. (A2), the conductance—and therefore the net conductance—is zero. This seems like a problem for Eq. (A18). On the other hand, the net conductance derived above [Eq. (A15)] is independent of R_m, and in the limit $R_m \to 0$, the circuits are equivalent.

Taking the limit of Eq. (A14), we find

$$\lim_{Q\to\infty} G_{\pm}(\omega) = \frac{\pi\omega_s^2 C_m}{2}\delta(\omega \mp \omega_0)\,. \tag{A22}$$

In this limit, the admittance in Eq. (A9) becomes

$$\begin{aligned} Y(\omega) = &-i\omega C_0 + i\frac{\omega_s^2 C_m}{2}\left[\frac{1}{\omega-\omega_s} + \frac{1}{\omega+\omega_s}\right] \\ &+ \frac{\pi\omega_s^2 C_m}{2}\left[\delta(\omega-\omega_s) + \delta(\omega+\omega_s)\right], \end{aligned} \tag{A23}$$

from which Eq. (A18) follows.

In contrast to Eq. (A2), the expression above satisfies the Kramers-Kronig relations. For any causal circuit, the susceptance $\chi(\omega) \equiv -\text{Im}\, Y(\omega)$ is related to $G(\omega)$ by [56]

$$\chi(\omega) = \frac{1}{\pi}P\int_{-\infty}^{\infty} d\omega'\,\frac{G(\omega')}{\omega'-\omega}, \tag{A24}$$

which the delta-function-pole pairs in Eq. (A23) satisfy.

3. Impulse response model of SAW transducer

The impulse response model (IRM) is a simple model of the piezoelectric transduction of a manifold of propagating modes—a band—rather than the resonant degrees of freedom described by the BVD circuit. The conductance of a transducer obtained from the IRM is $G(\omega) = G_+(\omega) + G_-(\omega)$, where [50]

$$G_+(\omega) = 8k^2_{\text{eff}} f_s C_0 N\frac{\sin^2 X}{X^2}, \tag{A25}$$

$X = \pi N(\omega-\omega_s)/\omega_s$, and $\omega_s = 2\pi f_s$. A similar expression follows for the negative-frequency response G_- centered at $-\omega_s$. Since

$$\int_{-\infty}^{\infty} dX\,\frac{\sin^2 X}{X^2} = \pi, \tag{A26}$$

we can integrate $G(\omega)$ around ω_s, changing variables from ω to X, to find

$$\int d\omega\, G(\omega) = 16\pi {f_s}^2 C_0 k^2_{\text{eff}}. \tag{A27}$$

Again the static capacitance can be related to quantities in the main text, namely $C_0 = Ac_s$, from which it follows that

$$A = \frac{\pi}{4}\frac{1}{\omega_s^2 c_s k^2_{\text{eff}}}\int d\omega\, G(\omega)\,. \tag{A28}$$

This is Eq. (1).

4. Using the net conductance to evaluate the piezoelectric coupling coefficient

Equation (A18) expresses the piezoelectric coupling coefficient k^2_{eff} in terms of quantities that can be directly measured—$G(\omega)$, ω_s, and C_0—without any appeals to a model. This expression comes with a couple of caveats. The first is that it does not discriminate between dissipation from mechanisms such as ohmic loss and dissipation from radiation into mechanical waves. If Eq. (A18) is used to calculate k^2_{eff}, care has to be taken to exclude nonmechanical loss mechanisms. Second, the interval of integration for the net conductance $\int d\omega\, G(\omega)$ has to be chosen carefully. All modes of a resonator or bands of a SAW transducer in the interval will contribute to the piezoelectric coupling in Eq. (A18). Finally, Eq. (A18) is correct only to first order in $(\omega_p - \omega_s)/\omega_p$. For large coupling, it is better to use Eq. (A20) to compute the resonance-frequency ratio ω_s/ω_p, which can then be plugged into Eq. (A4).

APPENDIX B: EVALUATING k^2_{eff} FOR A UNIT CELL OF A WAVEGUIDE

In Sec. II, we begin our design process by using the piezoelectric coupling coefficient k^2_{eff} and the expression

described in Appendix A to estimate the area needed to match the transducer to 50 Ω. It is well known that SH waves in X-cut lithium niobate exhibit a large k^2_{eff}, and there are numbers for suspended films available [44]. For an arbitrary material stack and waveguide geometry, transducer design begins with a study of k^2_{eff}. Here we show how we calculate k^2_{eff} for a mode of a wavelength-scale transducer. These methods can be used to study the angle dependence of k^2_{eff} in anisotropic media, the coupling of different modes of a waveguide, or the influence of geometry such as waveguide dimensions and electrode thickness.

The unit cell of the transducer is shown in Fig. 6(a). Floquet boundary conditions are imposed on the faces normal to the direction of propagation $\hat{y}$. Here we study the Γ-point solution, and so the wave vector K along $\hat{y}$ is set to 0. The frequencies of the modes supported in the unit cell under this constraint are plotted in the bands shown in Fig. 1. We compute the admittance $Y(\omega)$ for this domain, setting the voltage across the IDT to 1 V and solving the inhomogeneous piezoelectric equations by the FEM.

Each mode gives rise to a pole in the susceptance, which can be fitted to extract the residue G_Σ/π and therefore k^2_{eff}. Here G_Σ is the contribution to the net conductance from the pole. Ignoring contributions from other modes, the susceptance takes the form

$$\chi(\omega) = \omega C_0 + \frac{G_\Sigma}{\pi}\frac{1}{\omega_s - \omega}. \tag{B1}$$

We can independently compute the static capacitance C_0 and the series resonance frequency ω_s and put the problem of finding G_Σ into the form of a linear regression.

The series resonance frequency ω_s for each mode can be computed by solving the same eigenvalue problem as that solved to compute the bands in Fig. 1. Here $f_s = 1.683$ GHz. The static capacitance C_0 can be extracted from $\chi(\omega)$ by fitting a line to the low-frequency response. The capacitance per unit cell is 1.339 fF. Then we rewrite

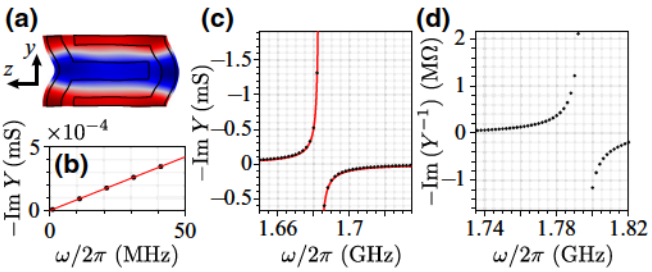

FIG. 6. (a) SH mode of a unit cell of the transducer. (b) Response near dc fitted for the static capacitance C_0. (c) The pole in the susceptance centered at the series resonance frequency f_s is fitted for the net conductance and used with C_0 to compute k^2_{eff}. (d) In addition to the pole in the admittance, there is a pole in the reactance centered at the parallel resonance frequency f_p.

Eq. (B1) as a linear regression

$$\frac{G_\Sigma}{\pi} = x \setminus y, \tag{B2}$$

with $y = \chi - \omega C_0$ and $x = (\omega_s - \omega)^{-1}$. This regression can be generalized to multiple modes by replacing x with a matrix X, where each column $(\omega_{s,i} - \omega)^{-1}$ corresponds to the ith pole, with frequency $\omega_{s,i}$.

From the fit in Fig. 6(c), we find $G_\Sigma = 32.91 \times 10^3$ S · Hz per unit cell. We can use G_Σ directly to compute the area needed to match the transducer to 50 Ω. By Eq. (A18), we find a k^2_{eff} of 17.26%. This approximate value for k^2_{eff} holds only to first order in $(\omega_p - \omega_s)/\omega_p$. If we want to use G_Σ to compute k^2_{eff} exactly, we can use the form in Eq. (A20) to find the resonance-frequency ratio ω_p/ω_s, which we plug into Eq. (A4) to find $k^2_{\text{eff}} = 14.70\%$.

There is an easier way to calculate k^2_{eff} for a unit cell directly in terms of ω_s and ω_p. In the absence of material loss, the admittance and reactance diverge at the series and parallel resonance frequencies, as seen in Figs. 6(c) and 6(d), respectively. A divergent admittance means that the voltage drop across the electrodes is zero. This is consistent with boundary conditions that short the IDT. By imposing these boundary conditions and solving for the eigenmodes of the unit cell at the Γ-point, we find $f_s = 1683$ MHz for the SH mode. This is the same frequency as that in the bands in Fig. 1(a). Similarly, the divergent impedance is consistent with an open terminal—floating boundary conditions for the electrodes—and, by solving for the eigenfrequency of the SH mode, we find $f_p = 1795$ MHz.

To first order in $(\omega_p - \omega_s)/\omega_p$, by Eq. (A8), we find

$$k^2_{\text{eff}} = \frac{\pi^2}{8}\left(\frac{\omega_p^2}{\omega_s^2} - 1\right) \tag{B3}$$

$$= 16.97\%, \tag{B4}$$

which can be used in Eq. (A1). This agrees well with the fit of the pole. Using ω_s/ω_p to compute k^2_{eff} from the definition [Eq. (A4)], we find $k^2_{\text{eff}} = 14.48\%$.

If material loss is added to the domain, the admittance and impedance no longer diverge, and the series and parallel resonances no longer correspond to shorted and open terminal boundary conditions on the electrodes. In such a case, the net conductance can be computed directly rather than by fitting the susceptance as described above.

We note that in a finite transducer, the wave excited by the transducer is only approximated by the Γ-point mode. The wave in a transducer exhibits a spatially varying envelope [45], in contrast to the Γ-point mode, which describes a uniform wave in an infinite transducer. The coupling

coefficient k^2_{eff} decreases away from the Γ-point because of mismatch between the wave vector K and the period of the electrodes a, and so this method gives us an upper bound on k^2_{eff}.

APPENDIX C: POWER DISSIPATION IN THE FOURIER DOMAIN

The voltage $V(t)$ can be expressed in the frequency domain as

$$V(\omega) = \frac{1}{2\pi}\int_{-\infty}^{\infty} dt\, V(t)e^{i\omega t}, \tag{C1}$$

and similarly for the current I and admittance Y. With our choice of Fourier convention, the power dissipated by an electrical element, $\mathcal{P}(t) = V(t)I(t)$, is the convolution of $V(\omega)$ and $I(\omega)$ in the frequency domain. Averaging this quantity in time extracts the dc component of the spectrum, thus reducing the convolution to

$$\langle\mathcal{P}\rangle = \int_{-\infty}^{\infty} d\omega\, V(\omega)I(-\omega). \tag{C2}$$

Since the voltage is a real-valued quantity, $V^*(\omega)$ is equal to $V(-\omega)$. (The same argument holds for $I(\omega)$ and $Y(\omega)$). Changing our limits of integration and using Ohm's law, $I(\omega) = Y(\omega)V(\omega)$, we find

$$\langle\mathcal{P}\rangle = \int_{0}^{\infty} d\omega\, [Y^*(\omega) + Y(\omega)]\, |V(\omega)|^2\,. \tag{C3}$$

Since $2\,\mathrm{Re}\,Y(\omega) = 2G(\omega) = Y(\omega) + Y^*(\omega)$, the time-averaged power dissipated by the electrodes is

$$\mathcal{P}_0 = 2\int_{0}^{\infty} d\omega\, G(\omega)\, |V(\omega)|^2\,. \tag{C4}$$

To determine the time-averaged power for a piezoelectric wave, we repeat the previous analysis starting from the instantaneous piezoelectric Poynting vector

$$\mathcal{P}_{\text{piezo}}(t) = -\boldsymbol{\sigma}(t)\mathbf{v}(t) + \Phi(t)\partial_t\mathbf{D}(t), \tag{C5}$$

and find the time-averaged piezoelectric power

$$\mathcal{P}_{\text{piezo}} = \int_{0}^{\infty} d\omega \int d\mathbf{S}\cdot(-\boldsymbol{\sigma}^*\mathbf{v} - \boldsymbol{\sigma}\mathbf{v}^* + i\omega\mathbf{D}^*\Phi - i\omega\mathbf{D}\Phi^*). \tag{C6}$$

We compare this expression with the inner product in Eq. (3) to confirm that $|a_m|^2$ is the time-averaged power in mode m. We note that our time-averaged power differs from that of Auld [46] by a factor of 1/4, resulting from differences in Fourier conventions. All values reported are power ratios, and thus factors of 2 from choices of convention drop out.

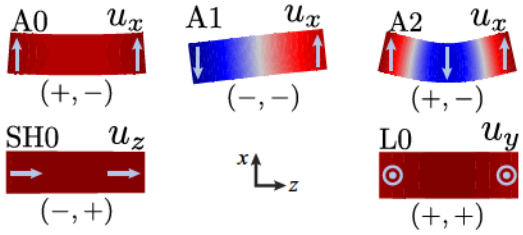

FIG. 7. Modes of a LN waveguide at 1.7 GHz. The colors in these plots visualize the dominant displacement field. Light blue arrows show the direction of displacement.

APPENDIX D: BASIS

Decomposition of the mechanical energy radiated into a waveguide is necessary for calculating the transmission coefficients such as $t_{b\mu}$ needed to characterize a phononic component. For completeness, we briefly describe the basis of propagating modes in a 300-nm-thick 1-μm-wide X-cut LN rectangular waveguide. We categorize the five 1.7-GHz modes as Lamb (A), horizontal shear (SH), and longitudinal (S) modes, which differ in their principal strains S_{xz}, S_{yz}, and S_{zz}, respectively. These modes are plotted in Fig. 7 along with their reflection symmetries (σ_z, σ_x), where $(+,-)$, for example, means symmetric and antisymmetric with respect to reflection across the x-y and y-z planes, respectively.

APPENDIX E: COMPUTING THE S-MATRIX

In our FEM analysis, we solve a set of inhomogeneous equations describing the behavior of our piezoelectric device. The drive term of these equations is a vector $(V, \mathbf{a}_-)^\top$, where V is the voltage across the leads of our transducer, and $\mathbf{a}_-$ is a vector of coefficients for the piezoelectric waves incident on the domain as defined by Eq. (4).

The solutions of these equations can be represented in matrix form,

$$\begin{pmatrix} I \\ \mathbf{a}_+ \end{pmatrix} = \begin{pmatrix} Y & \mathbf{x}_1^\top \\ \mathbf{x}_2 & \mathrm{X} \end{pmatrix}\begin{pmatrix} V \\ \mathbf{a}_- \end{pmatrix}. \tag{E1}$$

The scalar Y is the admittance of the transducer. For M modes, $\mathbf{x}_1$ and $\mathbf{x}_2$ are vectors with M components, and X is an $M \times M$ matrix. For the simulations reported here, the coefficients of $\mathbf{a}_-$ are set to 0, and we solve for the first column of the matrix in Eq. (E1) in terms of the input voltage V.

In order to study how these transducers behave in phononic networks—for example, the two-port transmission devices we use to measure $t_{b\mu}$—we want to transform the matrix in Eq. (E1) into a scattering matrix S. To do so, we reexpress V and I in terms of the microwave amplitudes

$a_{\pm\mu}$, which we abbreviate to $a_\pm$ in this section:

$$V = \sqrt{\frac{Z_0}{2}}\,(a_+ + a_-)\,, \tag{E2}$$

$$I = \frac{1}{\sqrt{2Z_0}}\,(a_- - a_+)\,. \tag{E3}$$

Here Z_0 is the impedance of the transmission line. Like a_m, the squares of the amplitudes a_+^2 and a_-^2 are the outward- and inward-going time-averaged power in the transmission line. This is easily checked by computing the power into the microwave port,

$$V^*I + VI^* = |a_-|^2 - |a_+|^2\,. \tag{E4}$$

By substituting Eqs. (E2) and (E3) into Eq. (E1) and collecting terms, we find the S-matrix

$$\begin{pmatrix} a_+ \\ \mathbf{a}_+ \end{pmatrix} = \underbrace{\begin{pmatrix} \dfrac{Y_0 - Y}{Y_0 + Y} & -\dfrac{\sqrt{2Y_0}}{Y_0 + Y}\mathbf{x}_1^\top \\ \dfrac{\sqrt{2Y_0}}{Y_0 + Y}\mathbf{x}_2 & \mathrm{X} + \dfrac{1}{Y_0 + Y}\mathbf{x}_2\mathbf{x}_1^\top \end{pmatrix}}_{S} \begin{pmatrix} a_- \\ \mathbf{a}_- \end{pmatrix}, \tag{E5}$$

where $Y_0 = Z_0^{-1}$. From reciprocity, $S = S^\top$, we find $\mathbf{x} \equiv \mathbf{x}_2 = -\mathbf{x}_1$ and therefore

$$\begin{aligned} S &= \begin{pmatrix} r_{\mu\mu} & t_{1\mu} & t_{2\mu} & \cdots \\ t_{1\mu} & r_{11} & t_{21} & \\ t_{2\mu} & t_{21} & r_{22} & \\ \vdots & & & \ddots \end{pmatrix} \\ &= \begin{pmatrix} \dfrac{Y_0 - Y}{Y_0 + Y} & \dfrac{\sqrt{2Y_0}}{Y_0 + Y}\mathbf{x}^\top \\ \dfrac{\sqrt{2Y_0}}{Y_0 + Y}\mathbf{x} & \mathrm{X} + \dfrac{1}{Y_0 + Y}\mathbf{x}\mathbf{x}^\top \end{pmatrix}. \end{aligned} \tag{E6}$$

The first component of S, connecting a_- and a_+, is the reflection S-parameter S_{11} in the absence of reflections in the network (such as off a second transducer). The component of S connecting a_- to the SH0 coefficient a_b is $t_{b\mu}$. Its magnitude is conveniently expressed as

$$|t_{b\mu}| = \sqrt{1 - |S_{11}|^2}\,\frac{|x_b|}{\sqrt{2G}}, \tag{E7}$$

where x_b is the SH0 component of $\mathbf{x}$ and is the coefficient a_b for a 1 V drive. $2G\,|V|^2$ is the total power dissipated by the transducer.

APPENDIX F: DEEMBEDDING $t_{b\mu}$, α, and r_{bb} FROM S_{21}

When making a transducer, especially one embedded in a network, e.g., a transducer coupled to a resonator, it is tempting to be satisfied with a well-matched S_{11}. Suppression of $|S_{11}|$, i.e., low microwave reflections, seems to imply that microwaves are being converted to mechanical waves and that the device is efficient. Under this prescription, one would choose an IDT's width and simply tune its length until it was matched. This procedure does not produce efficient devices.

A strong S_{11} dip is a *necessary* but insufficient condition for efficiency ($|t_{b\mu}|^2 \to 1$). In a microwave or phononic network, reflections can strongly modify the response of a component. Resonance can enhance the transmission through the device. If network performance is the prime and only concern, measuring a resonator's intracavity phonon number against the microwave input power, for example, will suffice. But if the goal is to make a transducer which can serve as a general component, one that can be embedded in an arbitrary network and the response accurately predicted, we need to deembed the transducer's response from the larger network response.

In Appendix E, we describe how the full scattering matrix S can be computed by the FEM. In Sec. IV, we show that the transmission into the SH0 mode exceeds the total transmission into all other modes by 10 dB. This allows us to reduce the S matrix of Eq. (E6) to that for two ports,

$$S = \begin{pmatrix} r_{\mu\mu} & t_{b\mu} \\ t_{b\mu} & r_{bb} \end{pmatrix}. \tag{F1}$$

The S-matrix for the waveguide is

$$S_{\mathrm{wg}} = \begin{pmatrix} e^{-\alpha L/2 - i\omega\tau} & 0 \\ 0 & e^{-\alpha L/2 - i\omega\tau} \end{pmatrix}, \tag{F2}$$

where $\tau = L/v_g$ is the transit time of the waveguide. The devices measured in Sec. V consist of a transducer, waveguide, and transducer. These components are cascaded in the signal-flow graph in Fig. 8(a), which can be reduced by standard methods [57] to find

$$S_{11} = r_{\mu\mu} + \frac{{t_{b\mu}}^2 r_{bb} e^{-\alpha L - 2i\omega\tau}}{1 - r_{bb}^2 e^{-\alpha L - 2i\omega\tau}} \tag{F3}$$

and

$$S_{21} = \frac{{t_{b\mu}}^2 e^{-\alpha L/2 - i\omega\tau}}{1 - r_{bb}^2 e^{-\alpha L - 2i\omega\tau}}, \tag{F4}$$

where ports 1 and 2 are the electrical ports of the first and the second transducer. The second term in our expression for S_{11} comes from reflections r_{bb} and gives rise to

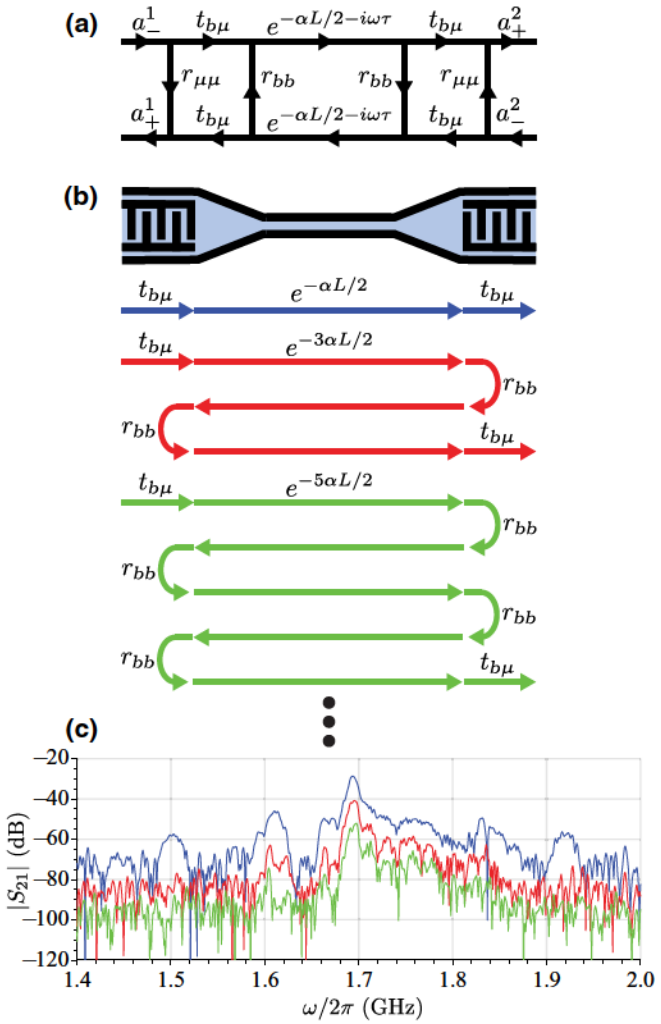

FIG. 8. (a) Signal-flow graph for a two-port device. (b) Paths for the single-, triple-, and quintuple-transit values (colored blue, red, and green, respectively) corresponding to the S_{21} curves of matching color in (c). (c) S_{21} filtered by path.

the Fabry-Perot peaks found on the blue side of ω_s in Fig. 4(c).

The impulse response $h(t)$ is computed by inverse Fourier transforming S_{21}. When $\left(1 - r_{bb}^2 e^{-\alpha L - 2i\omega\tau}\right)^{-1}$ is expanded to $\sum_n r_{bb}^{2n} e^{-n\alpha L - 2in\omega\tau}$, each term represents an echo in the impulse response in Fig. 4(e). These echoes and the paths they take are diagrammed in Fig. 8(b).

Since the $L = 800$ μm device is long enough to resolve the echoes, the amplitudes of the echoes can be analyzed directly in the frequency domain by filtering out each echo in Fig. 4(e) associated with a path in Fig. 8(b) and taking the Fourier transform. The results of this procedure are shown in the inset in Fig. 4(e) but are reproduced larger here for clarity. The transmission factor $|t_{b\mu}|^2 \exp(-\alpha L/2)$ is extracted from the first transit, plotted in blue.

APPENDIX G: INSERTION LOSS FROM IMPEDANCE MISMATCH

In Sec. V, we attribute a fraction of the insertion loss to an impedance mismatch between the transducers and transmission lines. This mismatch is labeled the *two-port mismatch* in Fig. 4(d). Derived below, this quantity is the average of the ratios of the power dissipated by each transducer to the incident microwave power, $1 - |S_{11}|^2/2 - |S_{22}|^2/2$.

For any lossy passive system,

$$|S_{11}|^2 + |S_{12}|^2 < 1 \tag{G1}$$

and

$$|S_{22}|^2 + |S_{21}|^2 < 1. \tag{G2}$$

Summing these conditions and assuming reciprocity, i.e., $S_{21} = S_{12}$, we have

$$|S_{11}|^2 + |S_{22}|^2 + 2|S_{21}|^2 < 2. \tag{G3}$$

Rearranging the above equation, we get

$$|S_{21}|^2 < 1 - |S_{11}|^2/2 - |S_{22}|^2/2. \tag{G4}$$

The right-hand side, which sets an upper bound on S_{21}, is the two-port mismatch.

[1] D. A. Fuhrmann, S. M. Thon, H. Kim, D. Bouwmeester, P. M. Petroff, A. Wixforth, and H. J. Krenner, Dynamic modulation of photonic crystal nanocavities using gigahertz acoustic phonons, Nat. Photonics **5**, 605 (2011).

[2] O. Couto, Jr., S. Lazić, F. Iikawa, J. Stotz, U. Jahn, R. Hey, and P. Santos, Photon anti-bunching in acoustically pumped quantum dots, Nat. Photonics **3**, 645 (2009).

[3] D. A. Golter, T. Oo, M. Amezcua, K. A. Stewart, and H. Wang, Optomechanical Quantum Control of a Nitrogen-Vacancy Center in Diamond, Phys. Rev. Lett. **116**, 143602 (2016).

[4] S. J. Whiteley, G. Wolfowicz, C. P. Anderson, A. Bourassa, H. Ma, M. Ye, G. Koolstra, K. J. Satzinger, M. V. Holt, F. J. Heremans, *et al.*, Spin–phonon interactions in silicon carbide addressed by gaussian acoustics, Nat. Phys. **15**, 490 (2019).

[5] M. Weiler, H. Huebl, F. S. Goerg, F. D. Czeschka, R. Gross, and S. T. B. Goennenwein, Spin Pumping with Coherent Elastic Waves, Phys. Rev. Lett. **108**, 176601 (2012).

[6] L. Fan, C.-L. Zou, N. Zhu, and H. X. Tang, Spectrotemporal shaping of itinerant photons via distributed nanomechanics, Nat. Photonics **13**, 323 (2019).

[7] Q. Liu, H. Li, and M. Li, Electromechanical Brillouin scattering in integrated optomechanical waveguides, Optica **6**, 778 (2019).

[8] S. A. Tadesse and M. Li, Sub-optical wavelength acoustic wave modulation of integrated photonic resonators at microwave frequencies, Nat. Commun. **5**, 5402 (2014).

[9] D. B. Sohn, S. Kim, and G. Bahl, Time-reversal symmetry breaking with acoustic pumping of nanophotonic circuits, Nat. Photonics **12**, 91 (2018).

[10] M. Merklein, B. Stiller, K. Vu, S. J. Madden, and B. J. Eggleton, A chip-integrated coherent photonic-phononic memory, Nat. Commun. **8**, 574 (2017).

[11] A. Vainsencher, K. J. Satzinger, G. A. Peairs, and A. N. Cleland, Bi-directional conversion between microwave and optical frequencies in a piezoelectric optomechanical device, Appl. Phys. Lett. **109**, 033107 (2016).

[12] J. Bochmann, A. Vainsencher, D. D. Awschalom, and A. N. Cleland, Nanomechanical coupling between microwave and optical photons, Nat. Phys. **9**, 712 (2013).

[13] K. C. Balram, M. I. Davanço, B. R. Ilic, J.-H. Kyhm, J. D. Song, and K. Srinivasan, Acousto-Optic Modulation and Optoacoustic Gating in Piezo-Optomechanical Circuits, Phys. Rev. Appl. **7**, 024008 (2017).

[14] M. Forsch, R. Stockill, A. Wallucks, I. Marinković, C. Gärtner, R. A. Norte, F. van Otten, A. Fiore, K. Srinivasan, and S. Gröblacher, Microwave-to-optics conversion using a mechanical oscillator in its quantum ground state, Nat. Phys. **16**, 69 (2020).

[15] W. Jiang, R. N. Patel, F. M. Mayor, T. P. McKenna, P. Arrangoiz-Arriola, C. J. Sarabalis, J. D. Witmer, R. V. Laer, and A. H. Safavi-Naeini, Lithium niobate piezo-optomechanical crystals, Optica **6**, 845 (2019).

[16] C. J. Sarabalis, R. Van Laer, and A. H. Safavi-Naeini, Optomechanical antennas for on-chip beam-steering, Opt. Express **26**, 22075 (2018).

[17] G. S. MacCabe, H. Ren, J. Luo, J. D. Cohen, H. Zhou, A. Sipahigil, M. Mirhosseini, and O. Painter, Phononic bandgap nano-acoustic cavity with ultralong phonon lifetime, arXiv:1901.04129 (2019).

[18] M. Pechal, P. Arrangoiz-Arriola, and A. H. Safavi-Naeini, Superconducting circuit quantum computing with nanomechanical resonators as storage, Quantum Sci. Technol. **4**, 015006 (2018).

[19] C. T. Hann, C.-L. Zou, Y. Zhang, Y. Chu, R. J. Schoelkopf, S. M. Girvin, and L. Jiang, Hardware-Efficient Quantum Random Access Memory with Hybrid Quantum Acoustic Systems, Phys. Rev. Lett. **123**, 250501 (2019).

[20] K. J. Satzinger, Y. P. Zhong, H.-S. Chang, G. A. Peairs, A. Bienfait, M.-H. Chou, A. Y. Cleland, C. R. Conner, É. Dumur, J. Grebel, I. Gutierrez, B. H. November, R. G. Povey, S. J. Whiteley, D. D. Awschalom, D. I. Schuster, and A. N. Cleland, Quantum control of surface acoustic-wave phonons, Nature **563**, 661 (2018).

[21] P. Arrangoiz-Arriola, E. A. Wollack, Z. Wang, M. Pechal, W. Jiang, T. P. McKenna, J. D. Witmer, R. Van Laer, and A. H. Safavi-Naeini, Resolving the energy levels of a nanomechanical oscillator, Nature **571**, 537 (2019).

[22] M. V. Gustafsson, T. Aref, A. F. Kockum, M. K. Ekstrom, G. Johansson, and P. Delsing, Propagating phonons coupled to an artificial atom, Science **346**, 207 (2014).

[23] K. Fang, M. H. Matheny, X. Luan, and O. Painter, Optical transduction and routing of microwave phonons in cavity-optomechanical circuits, Nat. Photonics **10**, 489 (2016).

[24] R. N. Patel, Z. Wang, W. Jiang, C. J. Sarabalis, J. T. Hill, and A. H. Safavi-Naeini, Single-Mode Phononic Wire, Phys. Rev. Lett. **121**, 040501 (2018).

[25] T. Manzaneque, R. Lu, Y. Yang, and S. Gong, Low-loss and wideband acoustic delay lines, IEEE Trans. Microw. Theory Tech. **67**, 1379 (2019).

[26] E. Romero, R. Kalra, N. P. Mauranyapin, C. G. Baker, C. Meng, and W. P. Bowen, Propagation and Imaging of Mechanical Waves in a Highly Stressed Single-Mode Acoustic Waveguide, Phys. Rev. Appl. **11**, 064035 (2019).

[27] K. Lakin, G. Kline, and K. McCarron, High-Q microwave acoustic resonators and filters, IEEE Trans. Microw. Theory Tech. **41**, 2139 (1993).

[28] T. Manzaneque, R. Lu, Y. Yang, and S. Gong, in *2017 IEEE 30th International Conference on Micro Electro Mechanical Systems (MEMS)* (IEEE, Las Vegas, Nevada, 2017), p. 155.

[29] A. Y. Cleland, M. Pechal, P.-J. C. Stas, C. J. Sarabalis, E. A. Wollack, and A. H. Safavi-Naeini, Mechanical purcell filters for microwave quantum machines, Appl. Phys. Lett. **115**, 263504 (2019).

[30] M. Eichenfield, J. Chan, R. M. Camacho, K. J. Vahala, and O. Painter, Optomechanical crystals, Nature **462**, 78 (2009).

[31] M. S. Kang, A. Brenn, and P. St J. Russell, All-Optical Control of Gigahertz Acoustic Resonances by Forward Stimulated Interpolarization Scattering in a Photonic Crystal Fiber, Phys. Rev. Lett. **105**, 153901 (2010).

[32] C. G. Poulton, R. Pant, and B. J. Eggleton, Acoustic confinement and stimulated Brillouin scattering in integrated optical waveguides, J. Opt. Soc. Am. B **30**, 2657 (2013).

[33] R. Van Laer, B. Kuyken, D. Van Thourhout, and R. Baets, Interaction between light and highly confined hypersound in a silicon photonic nanowire, Nat. Photonics **9**, 199 (2015).

[34] E. A. Kittlaus, H. Shin, and P. T. Rakich, Large Brillouin amplification in silicon, Nat. Photonics **10**, 463 (2016).

[35] P. Ovartchaiyapong, K. W. Lee, B. A. Myers, and A. C. B. Jayich, Dynamic strain-mediated coupling of a single diamond spin to a mechanical resonator, Nat. Commun. **5**, 4429 (2014).

[36] R. H. Olsson III and I. El-Kady, Microfabricated phononic crystal devices and applications, Meas. Sci. Technol. **20**, 012002 (2009).

[37] S. Mohammadi and A. Adibi, On chip complex signal processing devices using coupled phononic crystal slab resonators and waveguides, AIP Adv. **1**, 041903 (2011).

[38] W. Fu, Z. Shen, Y. Xu, C.-L. Zou, R. Cheng, X. Han, and H. X. Tang, Phononic integrated circuitry and spin–orbit interaction of phonons, Nat. Commun. **10**, 2743 (2019).

[39] A. V. Korovin, Y. Pennec, M. Stocchi, D. Mencarelli, L. Pierantoni, T. Makkonen, J. Ahopelto, and B. D. Rouhani, Conversion between surface acoustic waves and guided modes of a quasi-periodic structured nanobeam, J. Phys. D: Appl. Phys. **52**, 32LT01 (2019).

[40] A. Siddiqui, R. H. Olsson, and M. Eichenfield, Lamb wave focusing transducer for efficient coupling to wavelength-scale structures in thin piezoelectric films, J. Microelectromech. Syst. **27**, 1054 (2018).

[41] W. Jiang, C. J. Sarabalis, Y. D. Dahmani, R. N. Patel, F. M. Mayor, T. P. McKenna, R. Van Laer, and A. H. Safavi-Naeini, Efficient bidirectional piezo-optomechanical transduction between microwave and optical frequency, arXiv:1909.04627 (2019).

[42] R. S. Weis and T. K. Gaylord, Lithium niobate: Summary of physical properties and crystal structure, Appl. Phys. A Solids Surf. **37**, 191 (1985).

[43] A. S. Andrushchak, B. G. Mytsyk, H. P. Laba, O. V. Yurkevych, I. M. Solskii, A. V. Kityk, and B. Sahraoui, Complete sets of elastic constants and photoelastic coefficients of pure and MgO-doped lithium niobate crystals at room temperature, J. Appl. Phys. **106**, 073510 (2009).

[44] I. Kuznetsova, B. Zaitsev, S. Joshi, and I. Borodina, Investigation of acoustic waves in thin plates of lithium niobate and lithium tantalate, IEEE Trans. Ultrason., Ferroelectr. Freq. Control **48**, 322 (2001).

[45] C. J. Sarabalis, Y. D. Dahmani, A. Y. Cleland, and A. H. Safavi-Naeini, S-band delay lines in suspended lithium niobate, J. Appl. Phys. **127**, 054501 (2020).

[46] B. A. Auld, *Acoustic Fields and Waves in Solids* (Robert E. Krieger Publishing Company, Malabar, Florida, 1990), 2nd ed., Vol. II.

[47] B. A. Auld, *Acoustic Fields and Waves in Solids* (Robert E. Krieger Publishing Company, Malabar, Florida, 1990), 2nd ed., Vol. I.

[48] G. Vidal-Alvarez, A. Kochhar, and G. Piazza, in *2017 IEEE International Ultrasonics Symposium (IUS)* (IEEE, Washington D.C., 2017), p. 1.

[49] Y. Yang, R. Lu, T. Manzaneque, and S. Gong, in *2018 IEEE/MTT-S International Microwave Symposium – IMS* (IEEE, Philadelphia, Pennsylvania, 2018), p. 563.

[50] C. S. Hartmann, D. T. Bell, and R. C. Rosenfeld, Impulse model design of acoustic surface-wave filters, IEEE Trans. Microw. Theory Tech. **21**, 162 (1973).

[51] K.-Y. Hashimoto, ed., *RF Bulk Acoustic Wave Filters for Communications* (Artech House, Norwood, Massachusetts, 2009), Chap. 3, p. 57.

[52] R. Aigner *et al.*, in *IEEE Int. Symp. Acoust. Wave. Dev. for Future Mobile Communication Syst.* (IEEE, Chiba, Japan, 2007).

[53] C.-M. Lin, T.-T. Yen, Y.-J. Lai, V. V. Felmetsger, M. A. Hopcroft, J. H. Kuypers, and A. P. Pisano, Temperature-compensated aluminum nitride Lamb wave resonators, IEEE Trans. Ultrason. Ferroelectr. Freq. Control **57**, 524 (2010).

[54] J. D. Larson, P. D. Bradley, S. Wartenberg, and R. C. Ruby, in *2000 IEEE Ultrasonics Symposium. Proceedings. An International Symposium (Cat. No. 00CH37121)* (IEEE, San Juan, Puerto Rico, 2000), Vol. 1, p. 863.

[55] F. V. Pop, A. S. Kochhar, G. Vidal-Alvarez, and G. Piazza, in *2017 IEEE 30th International Conference on Micro Electro Mechanical Systems (MEMS)* (IEEE, Las Vegas, Nevada, 2017), p. 966.

[56] G. B. Arfken and H. J. Weber, *Mathematical Methods for Physicists* (AAPT, Cambridge, Massachusetts, 1999).

[57] D. M. Pozar, *Microwave Engineering* (John Wiley & Sons, Inc., Hoboken, New Jersey, 2012), 4th ed.